

1 **Using hierarchical mesoporous Mg-Al LDH as a potential model to**
2 **precisely load BSA for biological application**

3 Xiaoxuan Li ^a, Luxin Liang ^a, Yanni Tan ^a, Qianli Huang ^a, Si Yang ^a, Yingtao Tian ^b,
4 Jixiang Zhou ^{c, **}, Hong Wu ^{a, *}

5 ^a State Key Laboratory of Powder Metallurgy, Central South University, Changsha
6 410083, P. R. China

7 ^b Engineering Department, Lancaster University, Lancaster, LA1 4YW, UK

8 ^c Department of Hepatobiliary Surgery, Xiangya Hospital, Central South University,
9 410008, P.R. China

10 E-mail: hwucsu@csu.edu.cn (Hong Wu), winterrap@163.com (Jixiang Zhou)

1 **Abstract:** Bovine serum albumin (BSA) is a familiar protein and often used as a
2 model drug to test the adsorption efficiency of material, while the cytotoxicity of
3 hybrid is overlooked. In the present study, we synthesized hierarchical mesoporous
4 flower-like Mg-Al layered double hydroxides (LDH) microspheres through anion
5 surfactant mediated hydrothermal method. The scanning electron microscopic images
6 demonstrated that 10S-LDH and 100S-LDH samples possessed a porous surface and
7 the porosity structure were affected by the concentration of anionic surfactant, i.e.
8 sodium dodecyl sulfonate (SDS). By being immersed in the BSA/phosphate buffer
9 solution (PBS) solution, the 100S-LDH had a loading capacity about 44.6 mg/g.
10 Compared to 1S-LDH and 10S-LDH, the SDS intercalated in 100S-LDH could form
11 the hydrogen bond with BSA molecules and promote the adsorption efficiency. In the
12 cytotoxicity test towards Raw264.7 cells, the hybrid of BSA and xS-LDH showed a
13 superior biocompatibility to the raw LDH materials. The SDS intercalated Mg-Al
14 LDH is expected to be used in the bioactive molecules delivery.

15

16 **Keywords:** LDH, SDS, BSA adsorption, cytotoxicity, bioactive material

1. Introduction

Due to the great potential in diagnosing, preventing and treating diseases, nanomaterial carriers have received enormous attention in the fields of drug delivery and related applications [1-4]. An ideal nanomaterial carrier should be able to encapsulate high-dose drugs, and remain stable under all physiological conditions, provide protection, prevent drug degradation during transportation in the body, and provide drug release in cells. More importantly, these nanomaterials should be biocompatible [5,6]. Layered double hydroxide (LDH), also known as hydrotalcite-like material, has a general chemical formula of $[M^{2+}_{1-x}M^{3+}_x(OH)_2]^{x+}[A^{n-}_{x/n}]^{x-} \cdot mH_2O$ and widely exists in nature, where M^{2+} and M^{3+} are divalent and trivalent metal cations, respectively, A^{n-} is an interlayer anion to balance charge and H_2O is the co-intercalated water molecules [7]. Due to the anion exchange ability and the memory effect, LDH has been widely used in purification [8-10], catalysis [11, 12], and electrochemistry [13]. More importantly, LDHs have a high surface-to-volume ratio, so that they can hold large molecules [14].

By incorporating biocompatible metallic elements, such as Mg [15], Al [16], Ca [17], Zn [18], et al., LDH can be used as excellent biomaterial in biomedical science [19], cancer curing [20] and drug delivery [21]. The LDHs combined with bioactive molecules, such as DNA [22], shRNA [23], siRNA [24], protein [25, 26] and peptide [27, 28], have been used in biomedical field. Hasanur et al. [23] synthesized Ca-Al LDH nanoparticles and intercalated shRNA into the interlayer by mixing at different mass ratios. This internalized LDH-shRNA hybrid had the potential to treat colon cancer. The ultra-small LDH nanosheets can efficiently transport peptide nucleic acid (PNA) into cancer cells [27]. Furthermore, Mg-Al LDH coated by chitosan was used as the oral delivery of protein antigens to protect it from acidic degradation [29]. The potential of LDH in biomedical applications is tremendous.

Traditionally, surfactants are used in LDH material synthesis for its regulation in morphology and size [30-32], by forming micelles in aqueous solution and promoting the 2D LDH flakes to self-assembly 3D structure with hierarchical pore and large

1 surface area, which greatly promotes adsorption. Recently, it has been reported that
2 the surfactant inserted into the LDH layers through hydrothermal process^[32] or anion
3 exchange^[33] could enhance the adsorption capacity of Mg-Al LDH to cationic dye.
4 Aman et al.^[34] synthesized Zn-Al LDH by urea hydrolysis method, and mixed the
5 as-prepared material with 0.17 M sodium dodecyl sulfonate (SDS) aqueous solution,
6 by which SDS was inserted into the interlayer of Zn-Al LDH. However, SDS inserted
7 by anion exchange method could not regulate morphology and significantly change
8 the lamellar structure of LDH.

9 Several growth factors, including bone morphogenetic proteins (BMPs), tumor
10 necrosis factor-alpha (TNF- α) and vascular endothelial growth factor (VEGF-1), are a
11 group of special proteins and have great function in bone regeneration^[35]. For its low
12 cost, small molecular weight and stable structure, researchers replaced growth factor
13 with bovine serum albumin (BSA) to investigate the influence of carrier on protein
14 structure in development of drug carriers^[26, 36-41]. BSA is the main soluble protein
15 with multiple physiological functions in the circulatory system^[42], and often used as
16 an additional nutrient in cell culture. However, the work about LDH adsorbing BSA is
17 still focused on the adsorption behavior and influences of experimental conditions on
18 the adsorption efficiency, such as pH value, initial protein concentration and the
19 buffer solution. For example, Nogueira et al.^[37] have synthesized Mg-Al LDH and
20 Zn-Al LDH and evaluated the BSA loading efficiency under different pH value. Rojas
21 et al.^[26] optimized the BSA adsorption and enhanced the colloidal stability by
22 adjusting the LDH interfacial properties with intercalated surfactant, SDS. The effect
23 of LDH-protein hybrids on protein activity and cell activity is crucial to its application
24 in bioactive drug delivery, however, to the best of our knowledge, only a few studies
25 on this topic can be found in the literature so far.

26 In this work, we synthesized hierarchical mesoporous Mg-Al LDH microspheres
27 through anionic surfactant (SDS) mediated hydrothermal method. The influence of
28 SDS on the morphology, particle size and specific surface area of Mg-Al LDH was
29 investigated. The BSA adsorption efficiency of as-synthesized LDH at different SDS
30 concentration was tested. The characterization of Mg-Al LDH before and after

1 loading BSA were studied by means of field emission scanning electron microscope
2 (Fe-SEM), transmission electron microscope (TEM), X-ray diffraction (XRD),
3 Fourier transform infrared spectrometer (FTIR) and N₂ adsorption-desorption
4 measurement. Mouse macrophage cells (Raw264.7) were selected as the model to
5 determine the effects of LDH-BSA hybrid on the cell cytotoxicity *in vitro* and the
6 loaded protein activity.

7

8 **2. Materials and methods**

9 2.1. Materials

10 All the reagents were used directly as received. Al(NO₃)₃·9H₂O and urea
11 (H₂NCONH₂) were acquired from Shanghai Experimental Reagent CO., Ltd.
12 Mg(NO₃)₂·6H₂O was the magnesium resource and provided by Xilong Science CO.,
13 Ltd. Sodium dodecyl sulfate (SDS, C₁₂H₂₅SO₄Na) and bovine serum albumin (BSA)
14 were supplied by Biofroxx. Phosphate buffer solution (PBS) was acquired from
15 Biosharp. Distilled water was used as solvent and anhydrous ethanol acted as template
16 remover.

17

18 2.2. Synthesis of Mg-Al LDH particles

19 The Mg-Al LDHs involving an ionic surfactant were prepared by hydrothermal
20 method. 2.058 g Mg(NO₃)₂, 1.529 g Al(NO₃)₃ and 1.6833 g urea were added into 100
21 mL distilled water, and stirred vigorously to be fully dissolved, marked as Solution A.
22 Solution B was SDS aqueous solution with different concentrations of 1, 10 or 100
23 mM. After that, 30 mL of each solution A and B were mixed and magnetic stirred for
24 30 min, forming a clear mixture. Then, the mixed solution was introduced to a 100
25 mL Teflon-lined stainless-steel autoclave and put in oven at 150°C for 24 h. After
26 complete reaction, the reacted products were cooled to the room temperature naturally
27 and collected by centrifugation and washed by anhydrous ethanol and distilled water
28 thoroughly. The washed products were put in a vacuum drying oven to remove the
29 extra water, ground into powder in an agate mortar, and named as xS-LDH (x=1, 10,

1 100) according to the involved concentration of SDS.

2

3 2.3. Batch adsorption experiments of BSA

4 The experiment of BSA adsorbing onto Mg-Al LDH was conducted by adding
5 50 mg as-synthesized sample into 20 mL BSA-PBS solution (1 mg/mL) in centrifuge
6 tube. At certain time intervals (1 h, 6 h, 12 h and 24 h), the tubes were centrifuged at
7 10000 rpm, and 200 μ L supernatant of each tube was collected and kept at 4°C for
8 determining the concentration of BSA through BCA Protein Assay Kit. The loading
9 efficiency q_e (mg/g) was calculated by below equation:

$$10 \quad q_e = \frac{(C_0 - C_t)V}{m} \quad (1)$$

11 where C_0 (mg/mL) and C_t (mg/mL) are the BSA concentrations at the beginning and
12 the specific time (1 h, 6 h, 12 h, 24 h), respectively. V (mL) stands for the solution
13 volume and m (mg) means the mass of the adsorbent. After immersion for 12 h, the
14 supernatant was removed by centrifugation, and the precipitate was dried in the
15 vacuum drying oven overnight, then collected for subsequent tests. The powders with
16 BSA were named as BSA-xS-LDH ($x=1, 10, 100$).

17

18 2.4. Characterization

19 A field emission scanning electron microscope (FE-SEM, Helios Nanolab G3
20 UC, FEI) equipped with an energy-dispersive X-ray spectrometry (EDS) analyzer was
21 used to analyze the morphology and elemental composition of the Mg-Al LDH
22 samples before and after adsorption. A transmission electron microscope (TEM,
23 Tecnai G2 20S-Twin, FEI) was employed to further observe the changes in
24 microscopic morphology.

25 The characteristic patterns of composition phase were examined by X-ray
26 diffractometer (XRD, Advance D8, Bruker), using Cu K_α radiation source at 2° min^{-1}
27 in 2θ range of 10° - 80° . The chemical bonds of Mg-Al LDH before and after loading
28 BSA were measured by a Fourier transform infrared spectrometer (FTIR, AVANCEIII
29 500M, Bruker Biospin) between 500 and 4000 cm^{-1} . The pore structure and surface

1 area were tested by N₂ adsorption-desorption measurement and
2 Brunauer-Emmett-Teller (BET) method, by using an automatic specific surface
3 analyzer (Monosorb, Quantachrome).

4

5 2.5. Cell culture

6 Mouse macrophage cells, Raw264.7, were supplied by China Infrastructure of
7 Cell Line Sources and cultured in high glucose Dulbecco's modified Eagle's medium
8 (HG-DMEM, HyClone, USA) with 9% fetal bovine serum (FBS, Gibco, USA) and 1%
9 penicillin/streptomycin (PS, Gibco, USA) in an incubator with 5% CO₂ at 37°C. The
10 culture medium was replaced every 2 days. Once the cells filled the culture dish at
11 approximately 80%, they were seeded in 48 well-plates for further test at a density of
12 20000 cells per well.

13

14 2.6. CCK-8 test

15 To determine the cytotoxicity of as-synthesized materials, a cell counting kit-8
16 (CCK-8) test was carried out. The 1S-LDH, 10S-LDH and 100S-LDH powders were
17 disinfected by ultraviolet lamp for 3 days before dispersed in the completed culture
18 medium, namely the conditional medium. After the cells were seeded in 48
19 well-plates for 1 day, the conditional medium was added at three concentrations of 5,
20 10 and 50 µg/mL. At incubation with sample-contained conditional medium for 1, 2
21 and 3 days, the culture medium containing 10% of CCK-8 (Dojindo, Japan) solution
22 was added into each well, followed by incubating at 37°C for 30 min. The solutions
23 were introduced into 96 well-plates and illuminated by an elisa reader (Perkin-Elmer,
24 USA) at 450 nm. To discuss how the adsorbed BSA influences the cytotoxicity of
25 materials, the test was repeated under exactly same condition and through the same
26 procedure, except substituting xS-LDH with BSA-xS-LDH.

27

28 2.7. Statistical analysis

29 In this work, data processing was resolved by one-way analysis of variance
30 (ANOVA) and comparisons with least significant difference (LSD). A value of p<0.05

1 was considered to be statistically significant.

2

3 **3. Results and discussion**

4 3.1. Characterization of xS-LDH powders

5 Fig. 1 presents SEM images of xS-LDH and the corresponding EDS spectra.

6 When the concentration of SDS was at 1 mM, the 1S-LDH sample exhibited a loose
7 intersected structure with hexagonal nanoplates, and the average size was about 4 μm .

8 When the concentration was up to 10 mM, the morphology of 10S-LDH transformed
9 to flower-like mesoporous microspheres, and the size of the open-pore structure was

10 about 30-50 nm. With the concentration further increased to 100 mM, there was no

11 significant change in the morphology of 100S-LDH sample, while the size of
12 open-pore decreased to 15-20 nm. This indicated that the morphology has a close

13 relationship with the concentration of SDS and its micelles number in aqueous

14 solution. It is well known that the critical micelle concentration (CMC) of SDS is
15 about 8 mM^[43] and CMC is the lowest concentration for surfactant to form micelles.

16 When the concentration (1 mM) is far below the CMC, SDS exists as single
17 molecules in water and forms little micelle, which lead to the loosely intersected

18 structure. When the concentration (10 mM) is close to the CMC, spherical micelles

19 are formed by SDS molecules, serving as a template to promote the formation of

20 flower-like mesoporous microspheres. However, if the addition of SDS is higher than

21 the CMC, the micelles exist massively in the solution with the hydrophobic head

22 groups electrostatically linking with each other, and hydrophilic tails pointing to the

23 solution and interaction with LDH nanospheres^[44, 45]. Thus, LDH nanospheres

24 crystallized and grew along the micelle interface.

25 The EDS spectra of 1S-LDH and 10S-LDH (Fig. 1d and Fig. 1e) showed that the

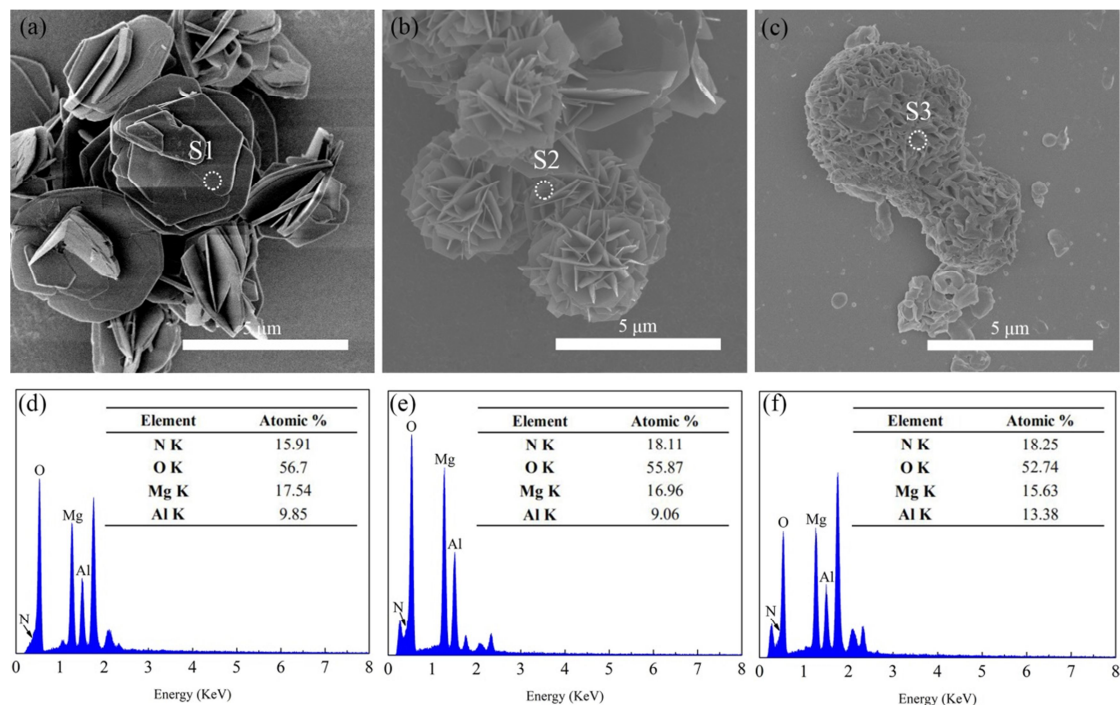
26 atomic ratio of Mg: Al was nearly 2 : 1, while the result of 100S-LDH (Fig. 1f)

27 showed the ratio was almost 1:1. Considering SDS is an anionic template and

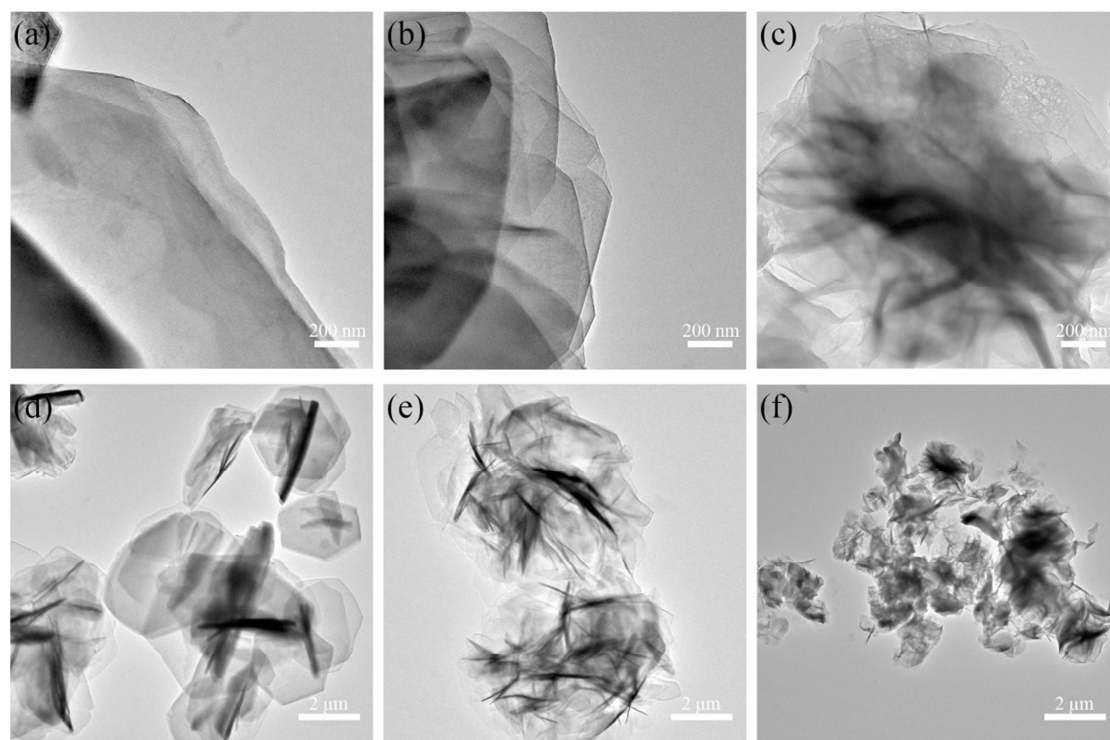
28 produces a hydrophilic end with negative charge in water, it combines with Al^{3+} more

29 easily when the concentration of SDS is higher than its CMC, which resulted in the

1 increase of Al^{3+} ratio in 100S-LDH. TEM patterns (Fig. 2) demonstrated the way how
 2 the LDH flakes combined together. With the increase of SDS concentration, the
 3 morphology changes from stacking horizontally to intersecting vertically.

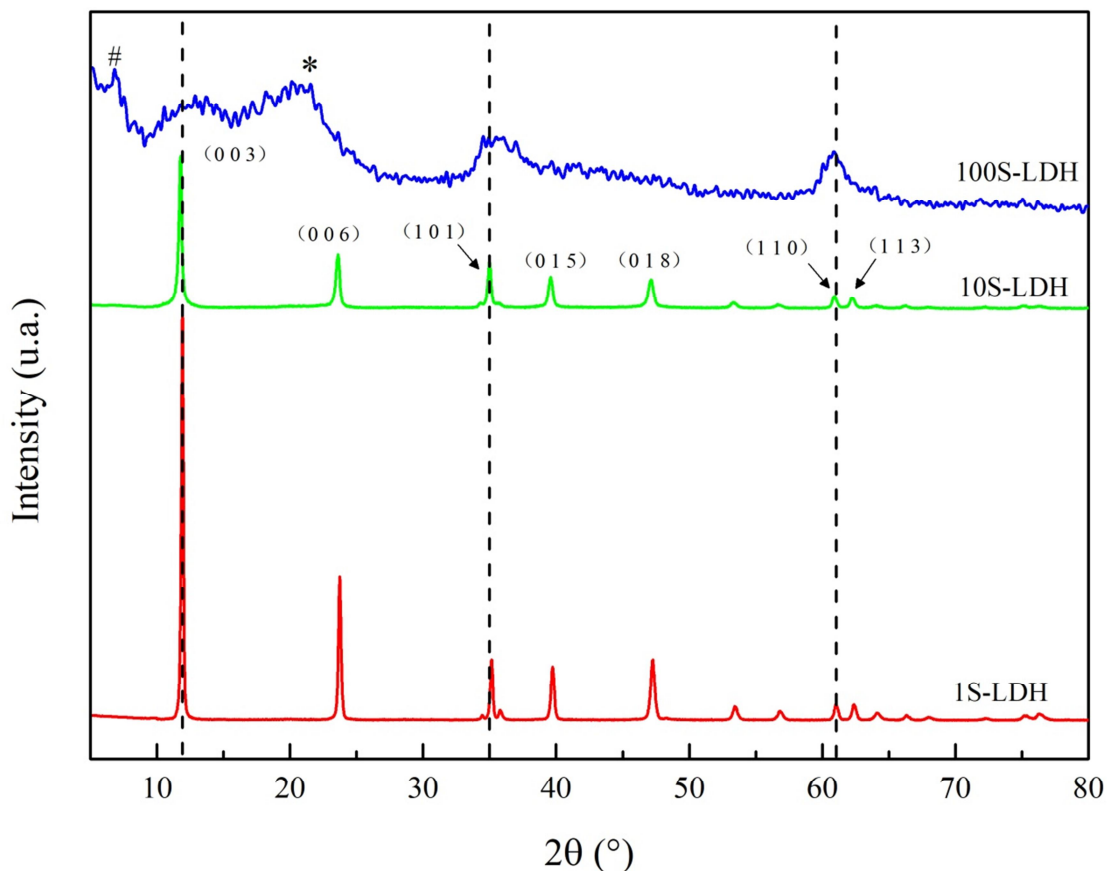


4
 5 Fig. 1. (a, b, and c) SEM images of 1S-LDH, 10S-LDH and 100S-LDH, and (d, e, and f) the corresponding EDS
 6 spectra.



7
 8 Fig. 2. TEM patterns of (a, d) 1S-LDH, (b, e) 10S-LDH and (c, f) 100S-LDH.

1 XRD patterns of the xS-LDH (x=1, 10, 100) are shown in Fig. 3. The 1S-LDH
 2 and 10S-LDH samples showed the same peaks at 11.91°, 23.74°, 34.36°, 39.74°,
 3 47.25°, 61.04°, 62.38°, which corresponded to the (0 0 3), (0 0 6), (1 0 1), (0 1 5), (0 1
 4 8), (1 1 0), (1 1 3) crystal planes, exhibiting all the characteristic diffractions of
 5 layered double hydroxides (JCPDS card No. 35-0964) [32], which indicated that these
 6 two samples are of hydrotalcite-like structure. The XRD pattern of 100S-LDH
 7 showed a near-amorphous structure with broad peaks at (0 0 3), (1 0 1) and (1 1 0),
 8 and the broad diffraction peak at $2\theta=20.5^\circ$ belongs to SDS (JCPDS card No. 39-1996,
 9 marked as “*”) [32]. According to the XRD results, the $d_{0\ 0\ 3}$ and $d_{1\ 1\ 0}$ values of
 10 1S-LDH were 7.42 Å and 1.51 Å, while the value of 100S-LDH increased to 7.50 Å
 11 and 1.52 Å, respectively, and the d spacing of 100S-LDH at $2\theta=6.87^\circ$ (marked as
 12 “#”) was 12.8 Å. The difference between 100S-LDH and other samples can be
 13 attributed to the fact that the SDS part is inserted into the LDH intermediate layer as
 14 an interlayer negative ion to balance the charge.



15 Fig. 3. XRD patterns of 1S-LDH, 10S-LDH and 100S-LDH.

17 N₂ adsorption-desorption tests were carried out, and the structural characteristics

1 are shown in Table 1. With the increase of SDS concentration from 1 mM to 10 mM,
 2 the specific surface area and mesoporous volume increased correspondingly. As the
 3 concentration further increased, the specific surface area and mesoporous volume
 4 decreased sharply, while the average pore size kept decreasing. When the
 5 concentration of SDS in the solution increased, LDH nanosheets were affected by the
 6 micelles in the solution and self-assemble into 3D flower-like microspheres, which
 7 greatly increased the BET surface area and mesoporous volume. When the
 8 concentration of SDS was further increased, the excessive number of micelles in the
 9 solution resulted in excessive aggregation of LDH nanosheets, so that the BET
 10 surface area and pore volume decreased. This reduction matches with the change in
 11 average mesoporous size, i.e. the mesoporous size decreased with the increasing
 12 density of LDH lamellae.

13 Table. 1. The textural properties of xS-LDH

Sample	BET surface area (m ² /g)	Pore volume (mm ³ /g)	BJH average pore size (nm)
1S-LDH	11.30	35.0	4.36
10S-LDH	24.21	118.2	3.42
100S-LDH	7.71	66.1	3.07

14 Fig. 4 shows the FTIR spectra of xS-LDH powders. For all samples without BSA
 15 adsorption, the peaks at 3450~3475 cm⁻¹, 1637 cm⁻¹, and 1078 cm⁻¹ correspond to
 16 stretching vibration of O-H bonds, physically adsorbed water, symmetric stretching
 17 vibration of NO₃⁻, respectively. The peaks at 686/553 cm⁻¹ resulted from the lattice
 18 vibrations of metal-oxygen. It should be pointed out that the peaks at 2919 cm⁻¹ and
 19 2850 cm⁻¹ correlate to the asymmetric γ_{as}(C-H) and symmetric γ_s(C-H) stretching
 20 modes of SDS, and the bending vibration δ(C-H) of SDS leads to the bands at 1467
 21 cm⁻¹ and 1384 cm⁻¹. The asymmetric γ_{as}(S=O) stretching at 1228 cm⁻¹ is another
 22 typical band of SDS. Besides, the presence of SDS caused a red shift on 100S-LDH
 23 sample around adsorption peaks at 1353 cm⁻¹, 944 cm⁻¹ and 782 cm⁻¹. Results of FTIR
 24 spectra are in accordance with the XRD patterns, indicating SDS intercalating into the
 25 LDH interlayer under the high surfactant concentration.

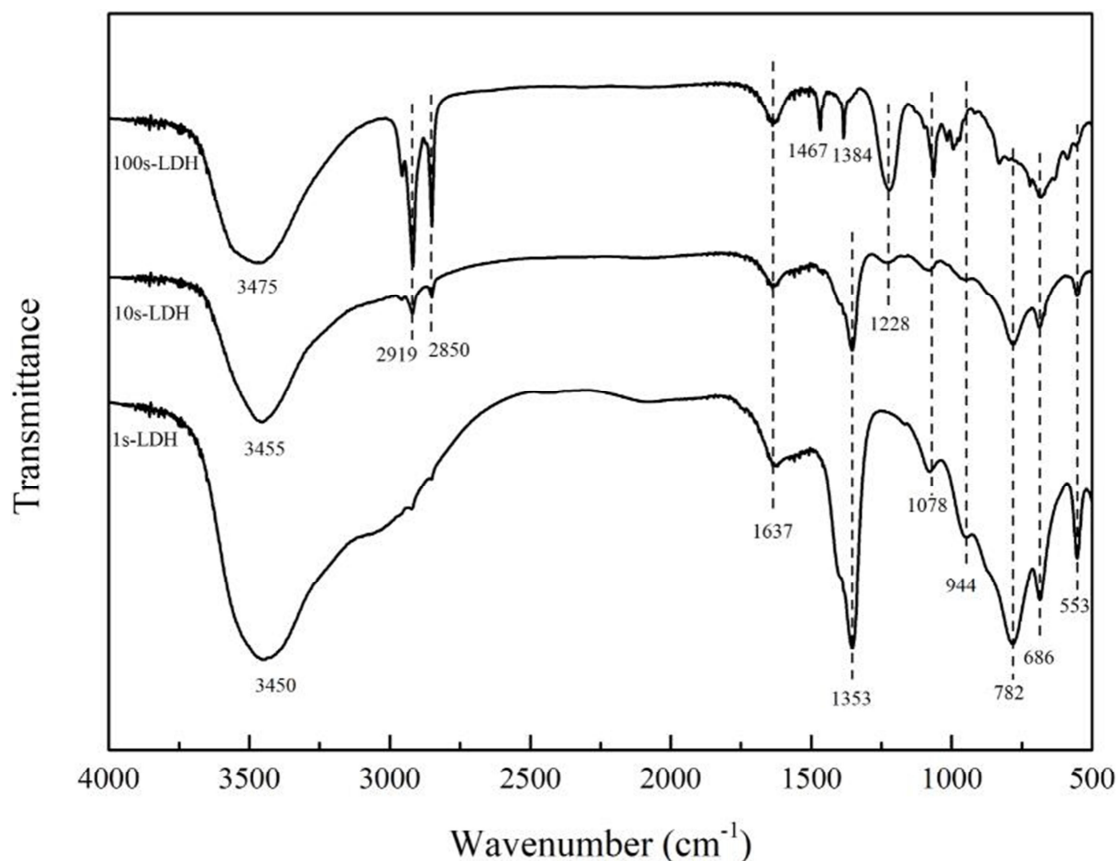
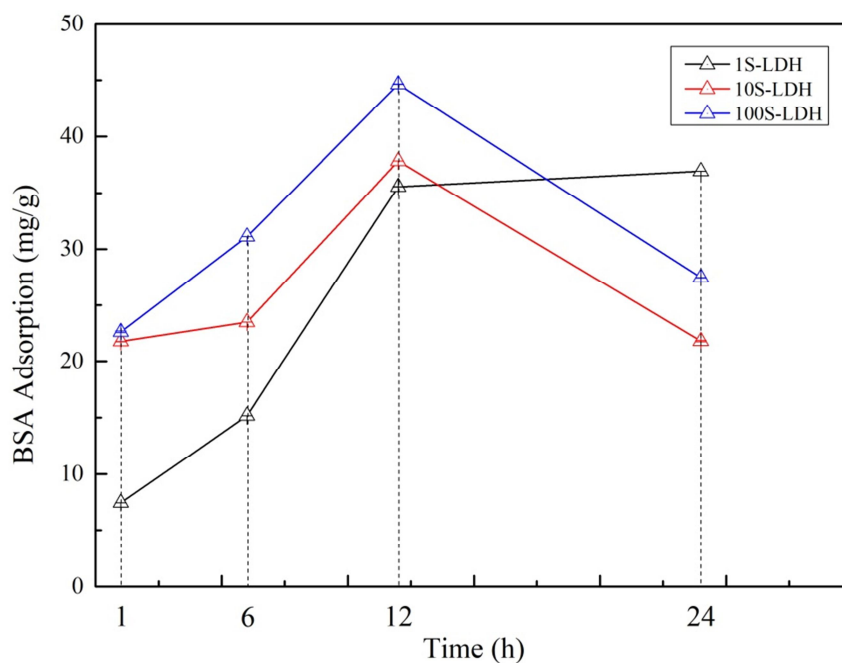


Fig. 4. FTIR spectra of xS-LDH (x=1, 10, 100).

3.2. Adsorption of BSA

The adsorption of BSA onto as-synthesized material was evaluated in a batch adsorption system to assess the influence of anionic template concentration. As shown in Fig. 5, the mass of adsorbed BSA in xS-LDH increased sharply over time for 12 h. For 24 h, the adsorbed content of 1S-LDH turned slowly, and the adsorbed contents of 10S-LDH and 100S-LDH decreased almost a half. Thus, the peak adsorption efficiency appeared around 12 h, and the maximum loadings for 1S-LDH, 10S-LDH and 100S-LDH were 35.6 mg/g, 37.8 mg/g and 44.6 mg/g, respectively. The adsorption efficiency of xS-LDH is better than those obtained in previous works [46, 47].



1

2

Fig. 5. Adsorption isotherms of BSA on xS-LDH (x=1, 10, 100).

3

4

5

6

7

8

9

Fig. 6 shows the FTIR spectra of BSA and BSA-xS-LDH powders. The FTIR spectrum of BSA showed the band at 3423 cm^{-1} , attributed to the $\delta(\text{N-H})$ bending vibration, and the band at 1654 and 1540 cm^{-1} , arising from $\gamma(\text{C=O})$ stretching (amide I), and the $\delta(\text{N-H})$ bending and $\gamma(\text{C-H})$ stretching (amide II). Comparing with xS-LDH samples, the red shift of BSA-xS-LDH sample occurred in the region from 1637 cm^{-1} to 1645 cm^{-1} . This revealed that the protein molecules were adsorbed and the hydrogen bonds between amide I of BSA and xS-LDH were formed.

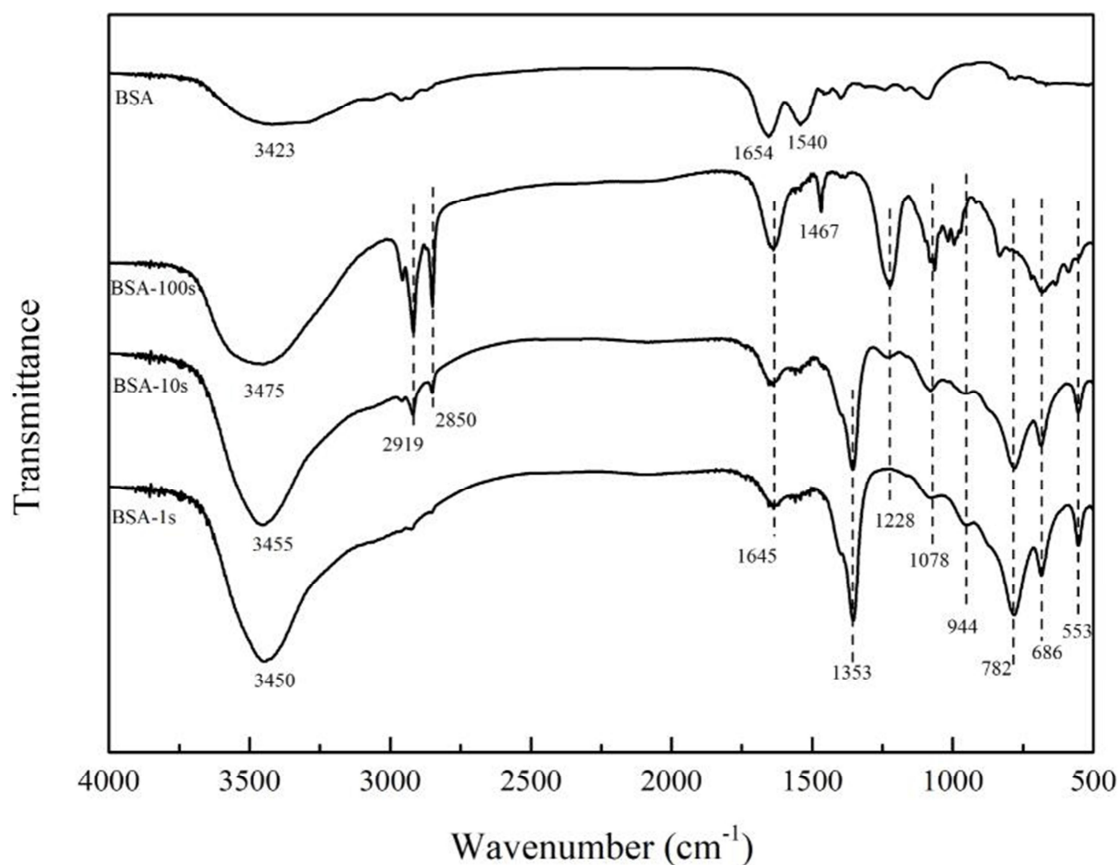
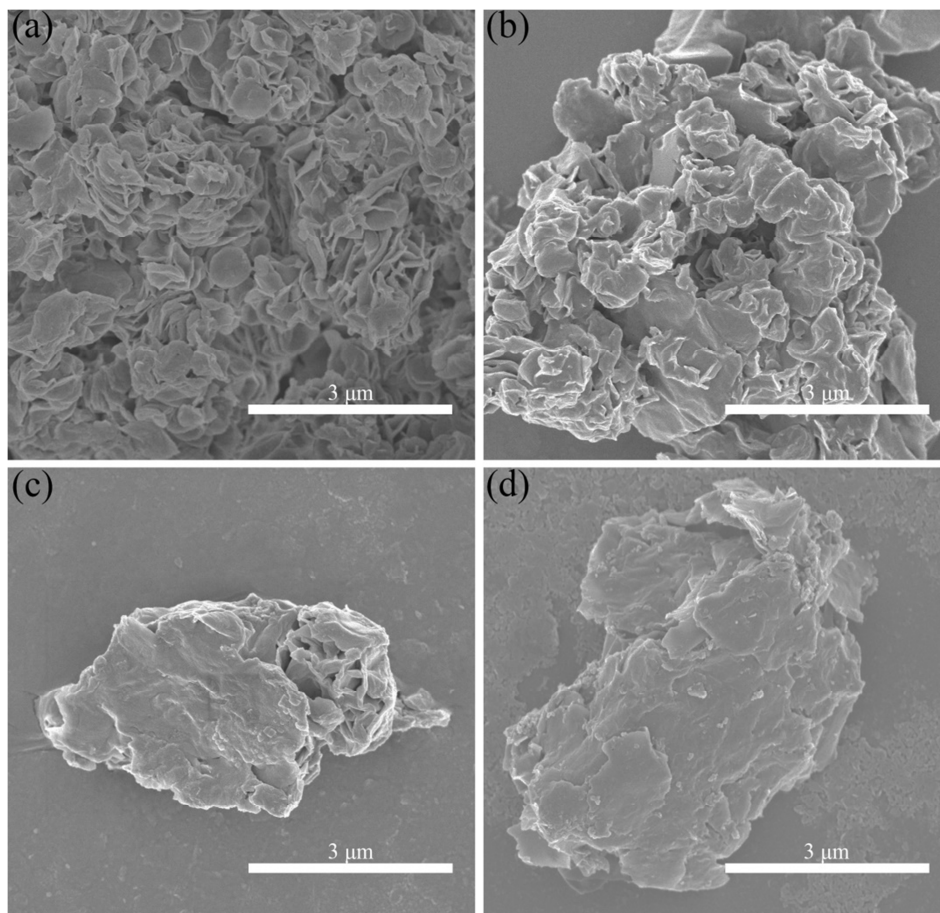


Fig. 6. FTIR spectra of BSA and BSA-xS-LDH (x=1, 10, 100).

Generally, there are three modes for nanoparticle to adsorb BSA, which are 1) the formation of chemical bond (chemisorption) between the surface of protein and adsorbents groups [48-51], 2) the electrostatic interactions between the surface of adsorbents and protein (physisorption) [52-55] and 3) the hydrophobic attraction between the adsorbents and protein [56]. Combining the above FTIR results, the BSA molecules were connected with xS-Mg-Al LDH through hydrogen bond. The decline of adsorption efficiency results from the replacement of intercalated SDS by anions in the solution, which makes the protein adsorbed on the material fall off. The 1S-LDH sample has little SDS, and the physisorption is dominant to its BSA adsorption partially, leading to a slow growth in adsorption efficiency rather than decline.

Fig. 7 shows that the mesoporous structure on the surface of 100S-LDH sample collapsed over time. When 100S-LDH powder was immersed in the BSA solution for 1 h, the structure maintained its original morphology well but the mesopore began to collapse after 6 h. Immersed for 12 h, about half the mesoporous structure remained while the other half was blocked by nanoflakes. When 100S-LDH powder was

1 immersed in the BSA solution for 24 h, nanohybrids BSA-100S-LDH presented an
2 aggregated compact morphology, resulting from the increase of adhesion among the
3 particles owing to the protein molecules. This evolution helps BSA molecules become
4 encapsulated in LDH particles, but hinders the subsequent adsorption.

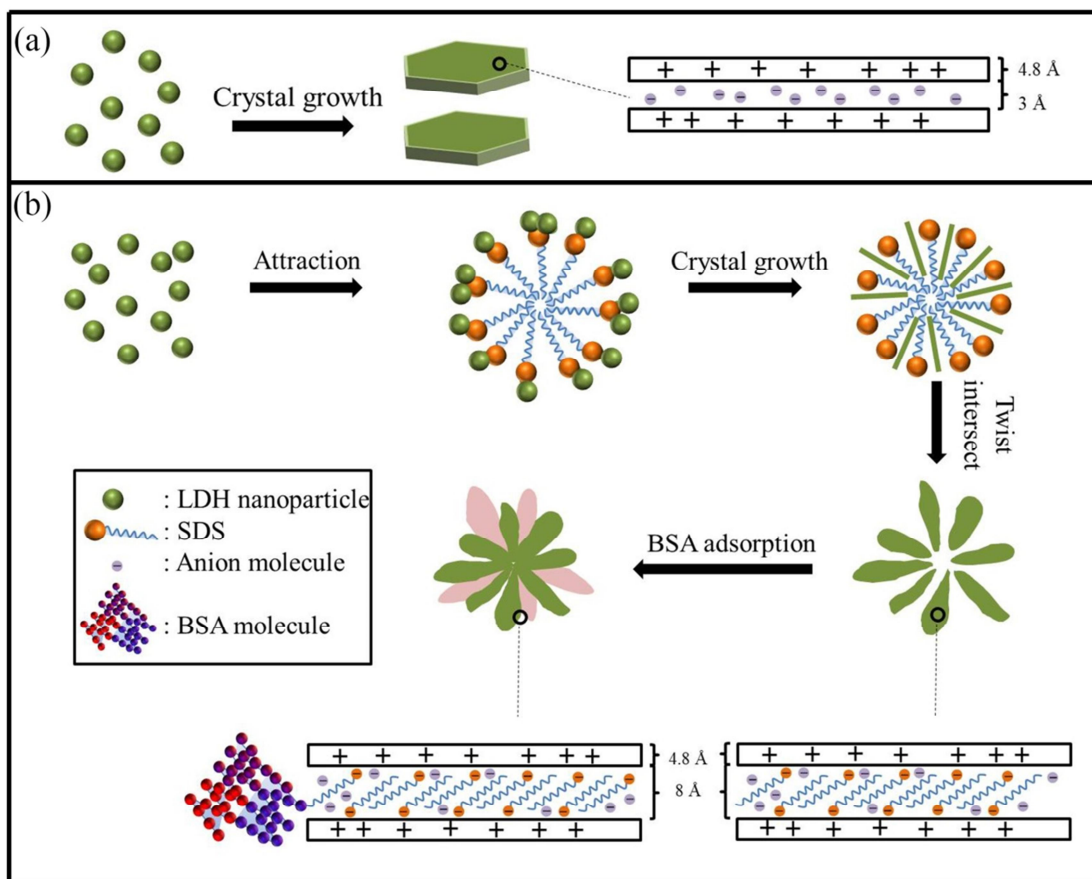


5
6 Fig. 7. SEM images of (a) 1h-100S-LDH, (b) 6h-BSA-100S-LDH, (c) 12h-BSA-100S-LDH and (d)
7 24h-BSA-100S-LDH.

8 The Schemes of formation mechanism for LDH synthesized without and with
9 SDS, and the scheme of BSA adsorption mechanism are shown in Fig. 8. The typical
10 LDH sheets have a thickness of 4.8 \AA ^[57], and the length of SDS chains is 15.3 \AA ,
11 based on Van der Waals radius ^[58]. According to the XRD result of 100S-LDH, the d
12 spacing at $2\theta=6.87^\circ$ is 12.8 \AA . Therefore, it can be calculated that the height of
13 interlayer is about 8 \AA , which is not suitable for SDS to intercalate vertically. Hence,
14 we infer that SDS exists in the interlayer with a tilt angle, and reveal the interaction
15 between anionic surfactant and LDH: SDS can spontaneously form micelles in
16 aqueous solution with the hydrophobic chains gathering together to shape the core and

1 the hydrophilic groups with negative charge pointing out to the solution. Once the
 2 LDH nanoflakes are formed, they are combined with the hydrophilic groups through
 3 charge attraction, and grow along the hydrophobic chains. In order to minimize the
 4 surface energy in the reaction, the LDH flakes aggregate and self-assemble into 3D
 5 hierarchical microspheres with an interlaced structure.

6 Considering that the BSA molecules ($40 \text{ \AA} \times 40 \text{ \AA} \times 140 \text{ \AA}$) have a relatively
 7 larger size than the interlayer space ^[25], it can be concluded that it is linked to the
 8 LDH microspheres by forming hydrogen bond with intercalated SDS, rather than
 9 inserting into the interlayer space.



10

11 Fig. 8. Schematic illustration of formation mechanism for (a) Mg-Al LDH without SDS and (b) Mg-Al LDH with

12

SDS and BSA adsorption mechanism.

13

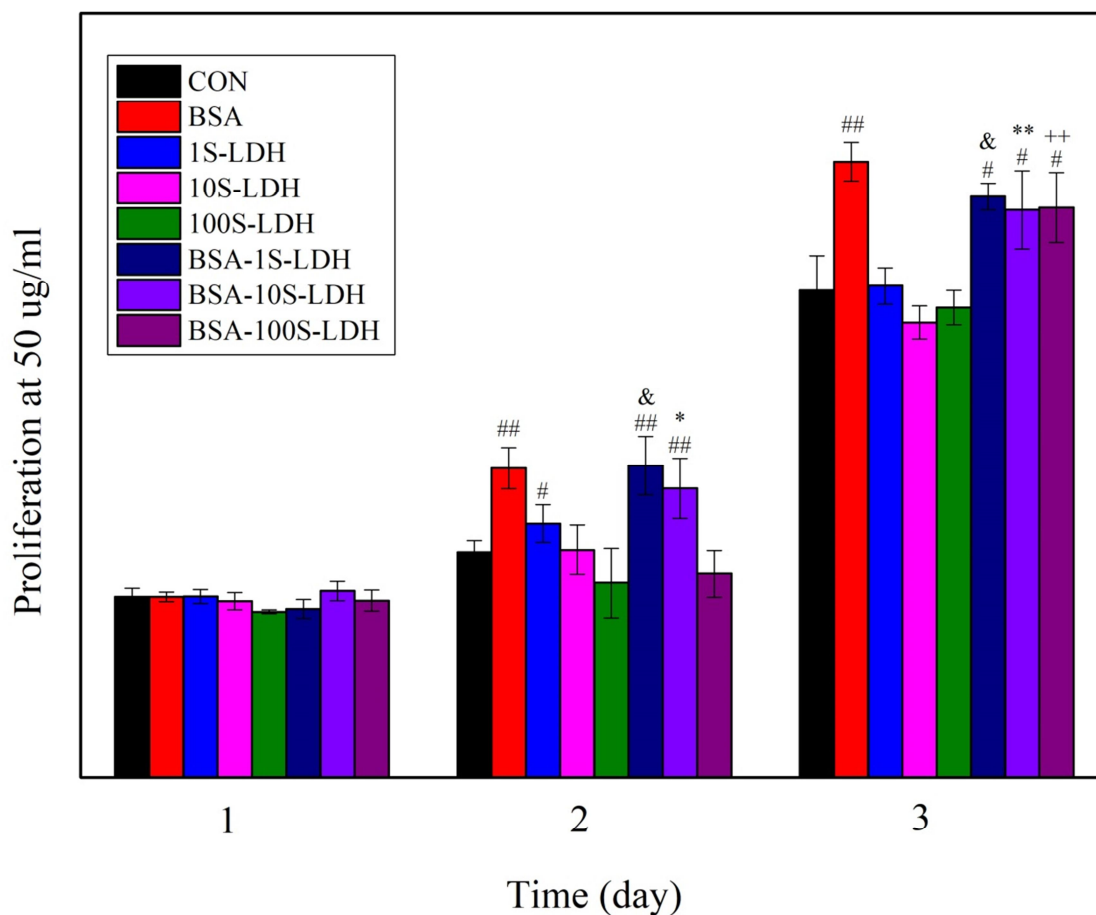
14 3.3. Cell Viability

15

16

The *in vitro* cytotoxicity of Raw264.7 cells cultured with samples was measured by CCK-8 test. As shown in Fig. 9, the cell proliferation had no significant difference

1 in each group for the first day, while both BSA-1S-LDH group and BSA-10S-LDH
 2 group promoted the cell proliferation compared to control group for the second day.
 3 The two groups also promoted the cell viability, in comparison with the 1S-LDH
 4 group and 10S-LDH group, respectively. On the third day, no significant difference
 5 was found between xS-LDH groups and the blank group. However, the cell
 6 proliferations of BSA-xS-LDH groups were greatly promoted, compared to the blank
 7 and xS-LDH group. The group co-incubated with 1 mg/mL BSA showed significant
 8 difference from blank group in day 2 and 3.



9
 10 Fig. 9. Cytotoxicity of xS-LDH and BSA-xS-LDH (x=1, 10, 100) samples under concentrations of 50 µg/mL at
 11 day 1, 2 and 3. #p < 0.05 and ##p < 0.01, compared with blank control. &p < 0.05, compared with
 12 1S-LDH. *p < 0.05 and **p < 0.01, compared with 10S-LDH. ++p < 0.01, compared with 100S-LDH

13 The xS-LDH samples have almost no *in vitro* cytotoxicity. This is because the
 14 cell viability is dependent on the released ion concentration. Liang et al. ^[59] reported
 15 that, with the increase of Mg²⁺ concentration, the cell proliferation was greatly
 16 promoted first but then deduced after certain point. It indicates the 50 µg/mL samples

1 are biocompatible. The significant difference between BSA group and blank group
2 ($p < 0.01$) showed that the presence of BSA in the culture medium can greatly promote
3 the cell proliferation. The addition of BSA improved the biocompatibility of LDH,
4 where the biocompatibility of BSA-LDH hybrids is much better than raw LDH
5 materials ($p < 0.05$). Bioactive molecules are utilized to improve the biocompatibility
6 of material, as they remain bioactive during loading process. The improvement of cell
7 proliferation in BSA-xS-LDH group indicates the combination of BSA with LDH has
8 no damage to the protein activity, which is consistent with previous studies. Rebekah
9 et al. ^[60] introduced chitosan into Fe-graphene oxide (GO) and promoted the
10 biocompatibility of Fe-GO-CS. The H1 peptide significantly improved the
11 biocompatibility of nanofibrous scaffolds ^[61].

12

13 **4. Conclusion**

14 The hierarchical mesoporous Mg-Al LDH microspheres were synthesized by
15 surfactant-assisted hydrothermal method. The anionic surfactant, SDS, was
16 successfully intercalated into the interlayer of Mg-Al LDH when it was up to 100 mM
17 in the solution, promoting the loading of BSA onto samples. The adsorption efficiency
18 of 100S-LDH reached the highest value of 44.6 mg/g at 12 h, subsequently the
19 adsorption of BSA into Mg-Al LDH were hindered due to the collapse of the
20 mesopores. The mechanism of adsorption is considered to be the combination of
21 hydrogen bonds between BSA and Mg-Al LDH. The *in vitro* biocompatibility test
22 results showed that the as-synthesized Mg-Al LDH barely had any cytotoxicity
23 towards Raw264.7 cells, and the BSA adsorbed into Mg-Al LDH greatly increased the
24 cell proliferation. The hybrid BSA-LDH has a potential application as bioactive drug
25 carrier, especially for protein and peptide.

26

27 **Acknowledgement**

28 This work was supported by the National Natural Science Foundation of China
29 (Grant No. 52071346) and the Changsha Municipal Natural Science Foundation

1 (Grant No. kq2014293).

2

3 **References**

- 4 [1] MARKMAN J L, REKECHENETSKIY A, HOLLER E, et al. Nanomedicine therapeutic
5 approaches to overcome cancer drug resistance [J]. *Advanced Drug Delivery Reviews*, 2013, 65(13-14):
6 1866-1879.
- 7 [2] GUO Z, LU J, WANG D, et al. Galvanic replacement reaction for in situ fabrication of
8 litchi-shaped heterogeneous liquid metal-Au nano-composite for radio-photothermal cancer therapy [J].
9 *Bioactive Materials*, 2021, 6(3): 602-612.
- 10 [3] YANG S, LIANG L, LIU L, et al. Using MgO nanoparticles as a potential platform to precisely
11 load and steadily release Ag ions for enhanced osteogenesis and bacterial killing [J]. *Materials Science*
12 *& Engineering C*, 2021, 119: 1-10.
- 13 [4] SUN H, ESWOTHY T, ROBERT K P, et al. Experimental and theoretical studies of tumor growth
14 [J]. *Journal of Micromechanics and Molecular Physics*, 2019, 04(03): 1-22.
- 15 [5] NAGARAJ V J, SUN X, MEHTA J, et al. Synthesis, Characterization, and In Vitro Drug Delivery
16 Capabilities of (Zn, Al)-Based Layered Double Hydroxide Nanoparticles [J]. *Journal of*
17 *Nanotechnology*, 2015, 2015: 1-11.
- 18 [6] LAI X, ROBERTS E. Cytotoxicity effects and ionic diffusion of single-wall carbon nanotubes in
19 cell membrane [J]. *Journal of Micromechanics and Molecular Physics*, 2019, 04(03): 1-15.
- 20 [7] ZHANG F, SONG Y, SONG S, et al. Synthesis of magnetite-graphene oxide-layered double
21 hydroxide composites and applications for the removal of Pb(II) and 2,4-dichlorophenoxyacetic acid
22 from aqueous solutions [J]. *Applied Materials & Interfaces*, 2015, 7(13): 7251-7263.
- 23 [8] OTGONJARGAL E, KIM Y-S, PARK S-M, et al. Mn-Fe Layered Double Hydroxides for
24 Adsorption of As(III) and As(V) [J]. *Separation Science and Technology*, 2012, 47(14-15): 2192-2198.
- 25 [9] PSHINKO G I, PUZYRNAYA L N, KOSORUKOV A A, et al. Removal of U(VI) from Water
26 Media by Layered Doubled Hydroxides of Magnesium and Iron [J]. *Journal of Water Chemistry and*
27 *Technology*, 2017, 39(3): 138-142.
- 28 [10] BORGIALLO A, ROJAS R. Reactivity and Heavy Metal Removal Capacity of Calcium Alginate
29 Beads Loaded with Ca–Al Layered Double Hydroxides [J]. *ChemEngineering*, 2019, 3(22): 1-13.
- 30 [11] BUKHTIYAROVA M V, NUZHIDIN A L, BUKHTIYAROV A V, et al. Cu layered double
31 hydroxides as catalysts for N-methylation of p-anisidine: Influence of synthesis conditions [J].
32 *Catalysis Communications*, 2019, 127: 39-44.
- 33 [12] TERAMURA K, IGUCHI S, MIZUNO Y, et al. Photocatalytic Conversion of CO₂ in Water over
34 Layered Double Hydroxides [J]. *Angewandte Chemie*, 2012, 51(32): 8008-8011.
- 35 [13] ZHEN F Z, QUAN J W, MIN Y L, et al. A study on the structure and electrochemical
36 characteristics of a Ni/Al double hydroxide [J]. *Metals and Materials International*, 2004, 10(5):
37 485-488.
- 38 [14] ARRABITO G, BONASERA A, PRESTOPINO G, et al. Layered Double Hydroxides: A Toolbox
39 for Chemistry and Biology [J]. *Crystals*, 2019, 9(7): 1-22.
- 40 [15] SU J-L, TENG J, XU Z-L, et al. Biodegradable magnesium-matrix composites: A review [J].
41 *International Journal of Minerals, Metallurgy and Materials*, 2020, 27(6): 724-744.
- 42 [16] PENG F, WANG D, ZHANG D, et al. The prospect of layered double hydroxide as bone implants:

1 A study of mechanical properties, cytocompatibility and antibacterial activity [J]. *Applied Clay Science*,
2 2018, 165: 179-187.

3 [17] SAHA S, RAY S, ACHARYA R, et al. Magnesium, zinc and calcium aluminium layered double
4 hydroxide-drug nanohybrids: A comprehensive study [J]. *Applied Clay Science*, 2017, 135: 493-509.

5 [18] YIN Y, HUANG Q, LIANG L, et al. In vitro degradation behavior and cytocompatibility of
6 ZK30/bioactive glass composites fabricated by selective laser melting for biomedical applications [J].
7 *Journal of Alloys and Compounds*, 2019, 785: 38-45.

8 [19] HU H, WANG X B, XU S L, et al. Preparation and evaluation of well-defined hemocompatible
9 layered double hydroxide-poly(sulfobetaine) nanohybrids [J]. *Journal of Materials Chemistry*, 2012,
10 22(30): 15362-15369.

11 [20] LI L, QIAN Y, SUN L, et al. Albumin-stabilized layered double hydroxide nanoparticles
12 synergised combination chemotherapy for colorectal cancer treatment [J]. *Nanomedicine :
13 nanotechnology, biology, and medicine*, 2021, 34: 102369-102375.

14 [21] GAO X, CHEN L, XIE J, et al. In vitro controlled release of vitamin C from Ca/Al layered double
15 hydroxide drug delivery system [J]. *Materials Science and Engineering C*, 2014, 39: 56-60.

16 [22] HU H, XIU K M, XU S L, et al. Functionalized Layered Double Hydroxide Nanoparticles
17 Conjugated with Disulfide-Linked Polycation Brushes for Advanced Gene Delivery [J]. *Bioconjugate
18 Chemistry*, 2013, 24(6): 968-978.

19 [23] RAHAMAN S H, BHATTACHARJEE A, SAHA S, et al. shRNA intercalation in CaAl-LDH
20 nanoparticle synthesized at two different pH conditions and its comparative evaluation [J]. *Applied
21 Clay Science*, 2019, 171: 57-64.

22 [24] ZHANG H, OUYANG D, MURTHY V, et al. Hydrotalcite Intercalated siRNA: Computational
23 Characterization of the Interlayer Environment [J]. *Pharmaceutics*, 2012, 4(2): 296-313.

24 [25] MINNELLI C, LAUDADIO E, GALEAZZI R, et al. Encapsulation of a Neutral Molecule into a
25 Cationic Clay Material: Structural Insight and Cytotoxicity of Resveratrol/Layered Double
26 Hydroxide/BSA Nanocomposites [J]. *Nanomaterials*, 2019, 10(1): 1-18.

27 [26] ROJAS R, GIACOMELLI C E. Size-tunable LDH-protein hybrids toward the optimization of
28 drug nanocarriers [J]. *Journal of Materials Chemistry B*, 2015, 3(14): 2778-2785.

29 [27] YU Z, HU P, XU Y, et al. Efficient Gene Therapy of Pancreatic Cancer via a Peptide Nucleic Acid
30 (PNA)-Loaded Layered Double Hydroxides (LDH) Nanoplatfrom [J]. *Small*, 2020, 16(23): 1-10.

31 [28] NAKAYAMA H, WADA N, TSUHAKO M. Intercalation of amino acids and peptides into Mg-Al
32 layered double hydroxide by reconstruction method [J]. *International Journal of Pharmaceutics*, 2004,
33 269(2): 469-478.

34 [29] YU X, WEN T, CAO P, et al. Alginate-chitosan coated layered double hydroxide nanocomposites
35 for enhanced oral vaccine delivery [J]. *Journal of Colloid and Interface Science*, 2019, 556: 258-265.

36 [30] LI B, HE J. Multiple Effects of Dodecanesulfonate in the Crystal Growth Control and
37 Morphosynthesis of Layered Double Hydroxides [J]. *Journal of Physical Chemistry C*, 2008, 112:
38 10909-10917.

39 [31] VARGA G, SOMOSI Z, KONYA Z, et al. A colloid chemistry route for the preparation of
40 hierarchically ordered mesoporous layered double hydroxides using surfactants as sacrificial templates
41 [J]. *Journal of Colloid and Interface Science*, 2021, 581: 928-938.

42 [32] ZHU Z, XIANG M, LI P, et al. Surfactant-modified three-dimensional layered double hydroxide
43 for the removal of methyl orange and rhodamine B: Extended investigations in binary dye systems [J].
44 *Journal of Solid State Chemistry*, 2020, 288: 1-10.

- 1 [33] ZHANG B, DONG Z, SUN D, et al. Enhanced adsorption capacity of dyes by surfactant-modified
2 layered double hydroxides from aqueous solution [J]. *Journal of Industrial and Engineering Chemistry*,
3 2017, 49: 208-218.
- 4 [34] GROVER A, MOHIUDDIN I, MALIK A K, et al. Zn-Al layered double hydroxides intercalated
5 with surfactant: Synthesis and applications for efficient removal of organic dyes [J]. *Journal of Cleaner*
6 *Production*, 2019, 240: 1-10.
- 7 [35] SAFARI B, DAVARAN S, AGHANEJAD A. Osteogenic potential of the growth factors and
8 bioactive molecules in bone regeneration [J]. *International Journal of Biological Macromolecules*, 2021,
9 175: 544-557.
- 10 [36] GONDIM D R, CECILIA J A, SANTOS S O, et al. Influence of buffer solutions in the adsorption
11 of human serum proteins onto layered double hydroxide [J]. *International Journal of Biological*
12 *Macromolecules*, 2018, 106: 396-409.
- 13 [37] NOGUEIRA K A B, CECILIA J A, SANTOS S O, et al. Adsorption behavior of bovine serum
14 albumin on Zn-Al and Mg-Al layered double hydroxides [J]. *Journal of Sol-Gel Science and*
15 *Technology*, 2016, 80(3): 748-758.
- 16 [38] FAN T, ZHANG H, GUO S H. Bovine Serum Albumin Modified Mg-Al Layered Double Oxides
17 Nanohybrids: Preparation and Potential Application as Drug Carrier [J]. *Advanced Materials Research*,
18 2011, 396-398: 330-335.
- 19 [39] TROWS S, SCHERLIESS R. Carrier-based dry powder formulation for nasal delivery of vaccines
20 utilizing BSA as model drug [J]. *Powder Technology*, 2016, 292: 223-231.
- 21 [40] LEE S H, SONG J G, HAN H-K. Development of pH-responsive organic-inorganic hybrid
22 nanocomposites as an effective oral delivery system of protein drugs [J]. *Journal of Controlled Release*,
23 2019, 311: 74-84.
- 24 [41] JI L, ZHANG F, ZHU L, et al. An in-situ fabrication of bamboo bacterial cellulose/sodium
25 alginate nanocomposite hydrogels as carrier materials for controlled protein drug delivery [J].
26 *International Journal of Biological Macromolecules*, 2021, 170: 459-468.
- 27 [42] CARTER D C, HO J X. Structure of Serum Albumin [M]. *Lipoproteins, Apolipoproteins, and*
28 *Lipases*. Academic Press, Inc., 1994: 153-203.
- 29 [43] DE S, MANDAL S. Surfactant-assisted shape control of copper nanostructures [J]. *Colloids and*
30 *Surfaces A*, 2013, 421: 72-83.
- 31 [44] BURLATSKY S F, ATRAZHEV V V, DMITRIEV D V, et al. Surface tension model for surfactant
32 solutions at the critical micelle concentration [J]. *Journal of Colloid and Interface Science*, 2013, 393:
33 151-160.
- 34 [45] KRALCHEVSKY P A, DANOV K D, ANACHKOV S E, et al. Extension of the ladder model of
35 self-assembly from cylindrical to disclike surfactant micelles [J]. *Current Opinion in Colloid &*
36 *Interface Science*, 2013, 18(6): 524-531.
- 37 [46] SWAIN S K, SARKAR D. Study of BSA protein adsorption/release on hydroxyapatite
38 nanoparticles [J]. *Applied Surface Science*, 2013, 286: 99-103.
- 39 [47] PANG D, HE L, WEI L, et al. Preparation of a beta-tricalcium phosphate nanocoating and its
40 protein adsorption behaviour by quartz crystal microbalance with dissipation technique [J]. *Colloids*
41 *Surface B: Biointerfaces*, 2018, 162: 1-7.
- 42 [48] FACCI P, ALLIATA D, ANDOLFI L, et al. Formation and characterization of protein monolayers
43 on oxygen-exposing surfaces by multiple-step self-chemisorption [J]. *Surface Science*, 2002, 504(1-3):
44 282-292.

1 [49] SCHNYDER B, KOTZ R, ALLIATA D, et al. Comparison of the self-chemisorption of azurin on
2 gold and on functionalized oxide surfaces [J]. *Surface and Interface Analysis*, 2002, 34(1): 40-44.

3 [50] WENG Y J, HOU R X, LI G C, et al. Immobilization of bovine serum albumin on TiO₂ film via
4 chemisorption of H₃PO₄ interface and effects on platelets adhesion [J]. *Applied Surface Science*, 2008,
5 254(9): 2712-2719.

6 [51] REYMOND-LARUINAZ S, SAVIOT L, POTIN V, et al. Protein-nanoparticle interaction in
7 bioconjugated silver nanoparticles: A transmission electron microscopy and surface enhanced Raman
8 spectroscopy study [J]. *Applied Surface Science*, 2016, 389: 17-24.

9 [52] SALIS A, MEDDA L, CUGIA F, et al. Effect of electrolytes on proteins physisorption on ordered
10 mesoporous silica materials [J]. *Colloids and Surfaces B*, 2016, 137: 77-90.

11 [53] PARSONS D F, DUIGNAN T T, SALIS A. Cation effects on haemoglobin aggregation: balance
12 of chemisorption against physisorption of ions [J]. *Interface Focus*, 2017, 7(4): 1-7.

13 [54] MACHADO N B, MIGUEZ J P, BOLINA I C A, et al. Preparation, functionalization and
14 characterization of rice husk silica for lipase immobilization via adsorption [J]. *Enzyme and Microbial
15 Technology*, 2019, 128: 9-21.

16 [55] ZHANG L, HU D, SALMAIN M, et al. Direct quantification of surface coverage of antibody in
17 IgG-Gold nanoparticles conjugates [J]. *Talanta*, 2019, 204: 875-881.

18 [56] RABE M, VERDES D, SEEGER S. Surface-induced spreading phenomenon of protein clusters
19 [J]. *Soft Matter*, 2009, 5(5): 1039-1047.

20 [57] F.CAVANI, F.TRIFIRB, A.VACCARI. Hydrotalcite-Type Anionic Clays: Preparation, Properties
21 and Applications [J]. *Catalysis Today*, 1991, 11: 173-301.

22 [58] JUN WANG F Y, CAIFU LI, SHANGYING LIU, AND DEJUN SUN. Double Phase Inversion of
23 Emulsions Containing Layered Double Hydroxide Particles Induced by Adsorption of Sodium Dodecyl
24 Sulfate [J]. *Langmuir*, 2008, 24: 10054-10061.

25 [59] LIANG L, HUANG Q, WU H, et al. Stimulation of in vitro and in vivo osteogenesis by Ti-Mg
26 alloys with the sustained-release function of magnesium ions [J]. *Colloids and Surfaces B:
27 Biointerfaces*, 2021, 197: 111360.

28 [60] REBEKAH A, SIVASELVAM S, VISWANATHAN C, et al. Magnetic nanoparticle-decorated
29 graphene oxide-chitosan composite as an efficient nanocarrier for protein delivery [J]. *Colloids and
30 Surfaces A*, 2021, 610: 1-9.

31 [61] XU R, ZHANG Z, TOFTDAL M S, et al. Synchronous delivery of hydroxyapatite and connective
32 tissue growth factor derived osteoinductive peptide enhanced osteogenesis [J]. *Journal of Controlled
33 Release*, 2019, 301: 129-139.

34